



## A comparison between image and signal sharpness-based axial localization of ultrasound scatterers

Diamantis, Konstantinos; Dalgarno, Paul A.; Anderson, Tom; Jensen, Jørgen Arendt; Sboros, Vassilis

*Published in:*

Proceedings of 2019 IEEE 16th International Symposium on Biomedical Imaging

*Link to article, DOI:*

[10.1109/ISBI.2019.8759225](https://doi.org/10.1109/ISBI.2019.8759225)

*Publication date:*

2019

*Document Version*

Peer reviewed version

[Link back to DTU Orbit](#)

*Citation (APA):*

Diamantis, K., Dalgarno, P. A., Anderson, T., Jensen, J. A., & Sboros, V. (2019). A comparison between image and signal sharpness-based axial localization of ultrasound scatterers. In *Proceedings of 2019 IEEE 16th International Symposium on Biomedical Imaging* (Vol. 2019-April, pp. 1610-1613). IEEE.  
<https://doi.org/10.1109/ISBI.2019.8759225>

---

### General rights

Copyright and moral rights for the publications made accessible in the public portal are retained by the authors and/or other copyright owners and it is a condition of accessing publications that users recognise and abide by the legal requirements associated with these rights.

- Users may download and print one copy of any publication from the public portal for the purpose of private study or research.
- You may not further distribute the material or use it for any profit-making activity or commercial gain
- You may freely distribute the URL identifying the publication in the public portal

If you believe that this document breaches copyright please contact us providing details, and we will remove access to the work immediately and investigate your claim.

# A COMPARISON BETWEEN IMAGE AND SIGNAL SHARPNESS-BASED AXIAL LOCALIZATION OF ULTRASOUND SCATTERERS

Konstantinos Diamantis<sup>\*</sup> Paul A. Dalgarno<sup>\*</sup> Tom Anderson<sup>†</sup> Jørgen Arendt Jensen<sup>◇</sup> Vassilis Sboros<sup>\*</sup>

<sup>\*</sup>School of Engineering & Physical Sciences, Heriot-Watt University, EH14 4AS Edinburgh, UK

<sup>†</sup>Centre for Cardiovascular Science, The University of Edinburgh, EH16 4TJ Edinburgh, UK

<sup>◇</sup>Center for Fast Ultrasound Imaging, Department of Electrical Engineering, Technical University of Denmark, DK-2800 Lyngby, Denmark

## ABSTRACT

Current super-resolution ultrasound methods are mainly based on image processing. Sharpness-based localization is an alternative to such methods for scatterer localization in the axial direction, and can be implemented both using image and signal data. A 7-MHz, 192-element, linear array transducer ( $\lambda=212 \mu\text{m}$ ) and the Synthetic Aperture Real-time Ultrasound System (SARUS) were used to image a wire-target (point scatterer) at different depth positions. The method predicts a depth estimate and its difference from the true scatterer position demonstrates its accuracy. This average difference can be as low as  $27.41 \mu\text{m}$  (or  $\approx \lambda/8$ ) for the image-derived sharpness and drops to  $2.84 \mu\text{m}$  (or  $\approx \lambda/75$ ) when the signals are used. These figures were calculated for a 8 mm depth range, which can be extended subject to further processing. Intermediate processes between the raw ultrasound data acquisition and the image formation such as interpolation and logarithmic compression compromise the overall performance of the method when using image data. Such details may be significant when reconstructing micro-vessels of the order of tens of micrometres in diameter.

**Index Terms**— Axial localization, multiple focusing, normalized sharpness, super-resolution ultrasound, ultrasound scatterers

## 1. INTRODUCTION

Super-resolution ultrasound allows the reconstruction of the micro-vasculature by localizing individual contrast microbubbles (MBs) that are injected into the micro-circulation. The MBs are efficient point scatterers and by using MB localization algorithms, it was possible to acquire transcranial images of the vascular structure [1], and to achieve *in-vivo* imaging of rodent microvessels with diameters in the range of  $10 \mu\text{m}$  [2–4]. These algorithms in their vast majority depend on image processing, and provided images of resolution be-

yond the diffraction limit, which is comparable to the wavelength ( $\lambda$ ). However, there is consensus that signal processing can achieve greater precision due to several distortions associated to the image formation stage (i.e. quantization errors, interpolation, logarithmic compression), and subsequently to the localization algorithms (image binarization, thresholding, frame rejection) [5, 6].

While several beamforming methods aim to improve lateral resolution [7, 8], the use of multi-focal imaging combined with the simple metric of sharpness provided a viable solution to obtain high accuracy axial localization of ultrasound scatterers [9]. The method originates from biological microscopy [10, 11] where it has been used in particle tracking applications. The localization of a point scatterer is accomplished by the formation of overlapping sharpness curves (*S*-curves). These are created by using multiple foci during receive beamforming, by measuring the sharpness values from individual point-spread-functions (PSFs), and by plotting these sharpness values over depth [9, 12]. In [9] particularly, it was shown that using unfocused ultrasound transmission, and three fixed foci during the receive processing of the transducer element signals were adequate to achieve axial localization with an accuracy of  $\approx 10 \mu\text{m}$  over a depth range of 15 mm. The sharpness metric which is defined as the integrated square intensity over the emitter [13], can be calculated from images using pixel intensities or from the beamformed ultrasound signals, using signal amplitudes, hence resulting in two separate implementations of the method. The objective of this work is to compare the two implementations using either image or raw ultrasound data, explain the nature of their differences, and suggest further improvements to increase the achieved accuracy. This is accomplished by performing an experimental wire-target study.

## 2. METHODS

### 2.1. Sharpness-based Localization

The axial localization is achieved by combining the data from all *S*-curves using a maximum likelihood estimation (MLE) algorithm with a calibration standard. The MLE involves the

---

This work was supported by the Science and Technology Facilities Council (STFC-ST/M007804/1), by grant 82-2012-4 from the Danish Advanced Technology Foundation, and by B-K Ultrasound ApS.

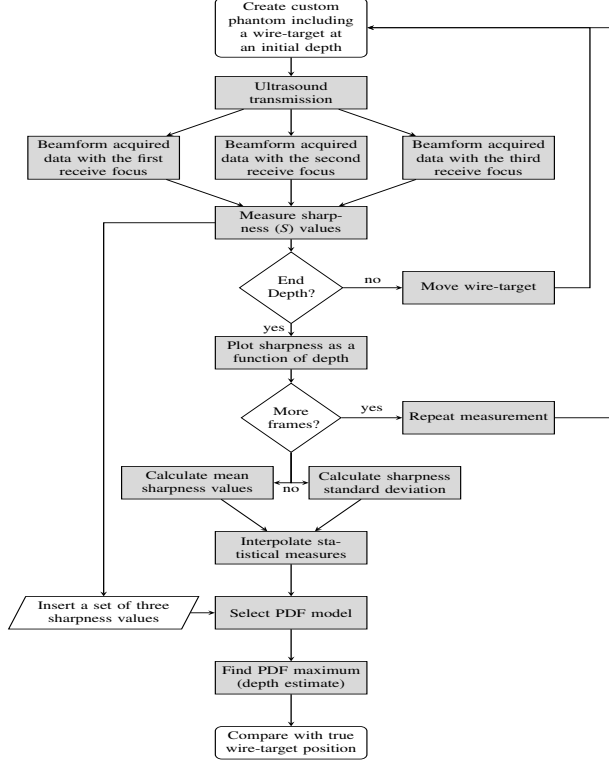


**Fig. 1.** Flow chart of ultrasound data acquisition and receive processing for the implementation of the normalized sharpness method.

sharpness data probability density function (PDF). This is a Gamma distribution showing the probability that a particular sharpness value will be measured at a particular depth and using a particular receive focus from the PSF of a point scatterer. The calibration standard consists of reference  $S$ -curves that are matched with the measured sharpness values. The reference data are obtained by performing repetitive sharpness measurements, by calculating the mean sharpness values and their standard deviations from these measurements, and by interpolating the statistical measures to provide adequate sampling. A flow-chart of the sharpness-based method is shown in Fig. 1, and a more detailed description can be found in [9]. In short, the element signals after scanning a point scatterer at a depth position are acquired and stored, and the acquisitions are repeated for a specific depth ( $z$ ) range. The raw ultrasound signals are then beamformed off-line with the conventional delay-and-sum (DAS) beamformer and fixed receive focusing. A normalized version of the sharpness metric is then calculated from a small region of interest (ROI) including the main-lobe of a single PSF, by:

$$S = \begin{cases} \sum_{k=1}^K n_k^2 / (\sum_{k=1}^K n_k)^2, & \text{using pixel intensity } (S_{int}), \\ \sum_{q=1}^Q |E_q|^4 / (\sum_{q=1}^Q |E_q|^2)^2, & \text{using signal envelope } (S_{env}), \end{cases}$$

where  $S$  is the normalized ultrasound sharpness measured

from either the recorded pixel intensities  $n_k$ , of  $K$  pixels in total ( $k = 1, \dots, K$ ), or from the squared envelope detected data amplitudes  $|E_q|^2$ , of  $Q$  samples ( $q = 1, \dots, Q$ ).

## 2.2. Experimental Setup

A copper wire with a diameter equal to 0.07 mm was mounted on the AIMS III positioning system (Onda Corporation, Sunnyvale, CA, USA) to create a custom phantom. The wire was attached to the positioning system between metal rods allowing it to be lowered into a water tank and to be moved in the axial direction. A 7-MHz, 192-element linear array was positioned above the wire in such way so that it is depicted as a point scatterer in the ultrasound image, and was then employed to scan the custom phantom. The initial wire position was  $(x, z) = (0, 40)$  mm. After an ultrasound transmission, the wire was moved to the next axial position using the high precision positioning system, which was controlled by a Matlab (MathWorks, Natick, MA, USA) interface. Data were produced between 32.5 mm and 47.5 mm from the transducer face (15 mm in total), in 139 steps with a distance ( $z$ -step) of  $108.7 \mu\text{m}$  between successive wire-target positions [9]. The speed of sound was calculated to  $c = 1484$  m/s based on the water temperature [14] and the wavelength was  $212 \mu\text{m}$ . All measurements were performed by the 1024 channel experimental Synthetic Aperture Real-time Ultrasound System (SARUS) [15], and the data were sampled at 35 MHz. The raw data from one plane wave (PW) emission were acquired from all 192 transducer elements individually in receive. The data acquisition was repeated 10 times for each wire-target axial position, resulting in 10 frames per position. All data were beamformed to three different foci in receive with the use of an in-house programmed beamformation toolbox BFT III [16]. The three receive foci were selected to be at 38 mm, 40 mm, and 42 mm respectively. The resulting sharpness data were interpolated by a factor of 1000.

## 2.3. Data Analysis

A set of three sharpness values as measured from a single wire-target data acquisition are used as input to the algorithm and the output is a depth position estimate. The accuracy of the normalized sharpness method is measured by the depth deviation of the method's  $z$ -estimate to the true scatterer position,  $d_{dev}$ . The true scatterer position is precisely known due to the AIMS III system described above. Depth estimates for all acquired datasets are predicted and compared with the actual positions. The  $d_{dev}$  results from the root mean square error (RMSE) from all 10 repetitive measurements. The normalized sharpness method does not perform uniformly for the whole displacement range [9] and the average  $d_{dev}$  is calculated for several smaller depth ranges, with the objective to exploit the areas where the rate of sharpness change is maximum ( $S$ -curves slopes). For this reason, the displacement edges, where the neighbouring sharpness values are similar,

are not taken into consideration during the  $d_{dev}$  calculation. The standard deviation  $d_{SD}$ , of the average  $d_{dev}$  is calculated as an extra indicator of the measurements' uncertainty.

### 3. RESULTS AND DISCUSSION

Fig. 2 shows five random PSFs corresponding to five different axial positions, where the receive focus was set to 40 mm, are shown as an example. The normalized sharpness was calculated by the pixels/raw signals included in the white box with dimensions  $2.3 \text{ mm} \times 2.3 \text{ mm}$  shown in Fig. 2(a). This region was represented by  $80 \times 80$  square pixels of image data while the matrix including the equivalent envelope detected data samples had dimensions  $22 \times 109$ . Hence the normalized sharpness calculation was different in the two cases resulting in different localization accuracy. In Fig. 3(a) a set of three image-derived  $S$ -curves are shown alongside the accuracy of the depth deviation to true scatterer position ( $d_{dev}$ ). In the figure, the peak sharpness value was measured to  $6.26 \times 10^{-6}$  around 38 mm depth for the curve corresponding to the shorter receive focus (38 mm), while the lowest sharpness value was  $3.22 \times 10^{-6}$  for the same curve. The latter value was equivalent to 51.4% of the peak sharpness and all measured sharpness values were within this range. This processing resulted in an average  $d_{dev}$  equal to  $63.67 \text{ } \mu\text{m}$  ( $\approx \lambda/3$ ) for the entire depth range between 32.5 mm and 47.5 mm. The  $d_{SD}$  for the same depths was calculated to  $102.35 \text{ } \mu\text{m}$  (or  $\approx \lambda/2$ ) due to the presence of several low precision estimates ( $\geq \lambda$ ) associated mainly to the wire-target displacement edges. The method's performance varied significantly with depth, and this led to  $d_{SD}$  being considerably higher than the average  $d_{dev}$ . Hence, a more reliable and improved result was obtained when the displacement edges were excluded from the average calculation. For the 8 mm depth range between 36 mm and 44 mm, the average  $d_{dev}$  reduced greatly to  $27.41 \text{ } \mu\text{m}$  ( $\approx \lambda/8$ ), with a similar  $d_{SD}$  ( $26.32 \text{ } \mu\text{m}$ ).

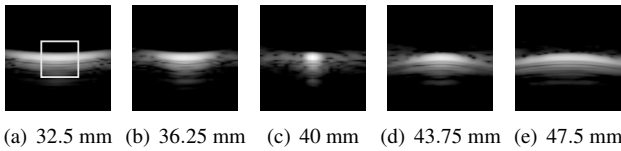


**Fig. 2.** Exemplary beamformed responses for five different axial wire-target positions during the experimental measurement. The receive focus was set to 40 mm, and the dimensions of each image were  $6 \text{ mm} \times 6 \text{ mm}$ . A 60 dB dynamic range of display was used. The normalized sharpness was calculated by the pixels/raw signal samples included in the box shown in (a).

Fig. 3(b) shows a set of three  $S$ -curves and the accuracy in the wire axial localization based on the signal-derived sharpness processing. In the figure, the peak sharpness value was measured to  $8.93 \times 10^{-3}$  around 38 mm depth for the curve corresponding to the shorter receive focus (38 mm), while the lowest sharpness value was  $3.68 \times 10^{-3}$  for the same curve, around 32.5 mm depth. The latter value was equivalent to

41.2% of the peak sharpness which demonstrates higher rate of sharpness change in the signal domain compared to image one. A high rate of sharpness change is a crucial characteristic for the method's performance [9]. Therefore this result highlights the advantage of assessing the sharpness values using the signal data. This advantage was translated to the wire depth position being consistently estimated with sub-wavelength precision. The signal processing resulted in an average  $d_{dev}$  equal to  $10.21 \text{ } \mu\text{m}$  ( $\approx \lambda/21$ ) for the entire depth range between 32.5 mm and 47.5 mm. The  $d_{SD}$  for the same depths was calculated to  $16.11 \text{ } \mu\text{m}$  (or  $\approx \lambda/13$ ). The above results further improved when the displacement edges were excluded from the average calculation. For the 8 mm depth range between 36 mm and 44 mm, the average  $d_{dev}$  reduced greatly to  $2.84 \text{ } \mu\text{m}$  ( $\approx \lambda/75$ ), with an equally low  $d_{SD} = 2.53 \text{ } \mu\text{m}$ .

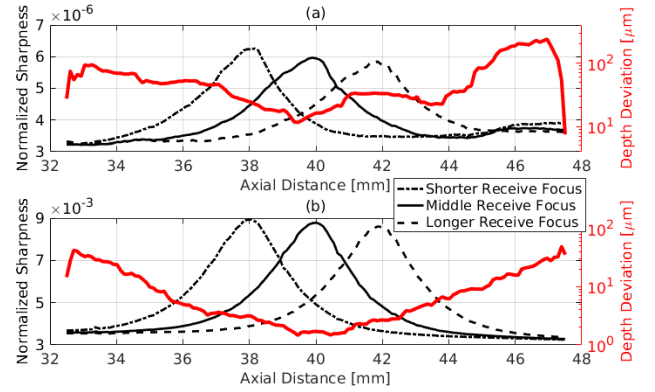


**Fig. 3.** A set of three (a) image- and (b) signal-derived  $S$ -curves from the wire-target moving in the axial direction. Data were generated by unfocused PW ultrasound transmission and by beamforming with three different foci in receive. The estimated depth deviation to the true wire-target position ( $d_{dev}$ ) is also plotted over axial distance in both (a) and (b) in red.

As outlined in [9], more than three foci in receive can be used to create more  $S$ -curves and cover an increased and more realistic penetration depth. Although this is not limited to a specific number, 11 foci were selected for the last part of this work and were combined with the sharpness data processing in the signal domain. The receive foci were set successively from 35 mm to 45 mm with 1 mm distance between them. The resulting  $S$ -curves can be found in Fig. 4(a), and the  $d_{dev}$  in Fig. 4(b), where the logarithmic scale in the y-axis was abandoned since no individual  $d_{dev}$  value higher than  $26 \text{ } \mu\text{m}$  ( $\approx \lambda/8$ ) was measured. From the Fig. 4(b), it is shown that increasing the number of  $S$ -curves further improved the results acquired previously. The smallest average  $d_{dev}$ , thus maximum accuracy, was calculated for a 4 mm area between 38 mm and 42 mm, and had a value equal to  $1.08 \text{ } \mu\text{m}$  ( $\approx \lambda/200$ ) with the  $d_{SD}$  being  $1 \text{ } \mu\text{m}$ . When a longer 13 mm distance was considered, from 33 mm up to 46 mm, the calculated average  $d_{dev}$  remained relatively low and was equal to  $2.87 \text{ } \mu\text{m}$  ( $\approx \lambda/74$ ) with a similar  $d_{SD}$  ( $2.85 \text{ } \mu\text{m}$ ). Thus, by

increasing the number of  $S$ -curves it was possible to extend the super-resolution axial localization accuracy for almost the entire displacement range.

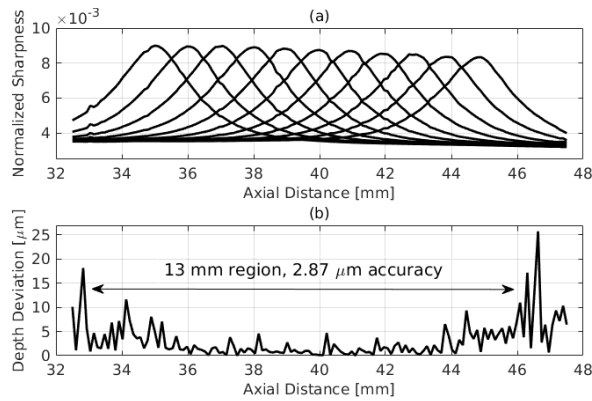


**Fig. 4.** (a) A set of eleven normalized  $S$ -curves from the wire target moving in the axial direction. Data were generated by unfocused PW ultrasound transmission and by beamforming with eleven different foci in receive. Eleven sharpness values for each scatterer position result in average  $d_{dev}$  equal to  $2.87 \mu\text{m}$  for a 13 mm distance as shown in (b).

#### 4. CONCLUSION

Two implementations of the normalized sharpness method involving image and raw signal data, for the precise axial localization of ultrasound scatterers were examined and compared in-depth, using experimental wire-target data. The method exploits the distinctive behaviour of a scatterer as it moves through the axial direction, and attempts to link the metric of sharpness with the axial position. The performance of the method was found to be dependent on the rate of sharpness change, the depth range of interest, and the number of overlapping sharpness curves, and may provide axial localization with accuracy improved by two orders of magnitude compared to that achieved by conventional imaging. The signal processing resulted in almost tenfold localization accuracy gains compared to the image processing, and it is suggested that it should be preferred not only for the particular method but for super-resolution related applications in general.

#### 5. REFERENCES

- [1] M. A. O'Reilly, R. M. Jones, and K. Hynynen, "Three-dimensional transcranial ultrasound imaging of microbubble clouds using a sparse hemispherical array," *IEEE Trans. Biom. Eng.*, vol. 61, no. 4, pp. 1285–1294, 2014.
- [2] K. Christensen-Jeffries, R. J. Browning, M. X. Tang, C. Dunsby, and R. J. Eckersley, "In vivo acoustic super-resolution and super-resolved velocity mapping using microbubbles," *IEEE Trans. Medical Imaging*, vol. 34, no. 2, pp. 433–440, Feb. 2015.
- [3] C. Errico, B. F. Osmanski, S. Pezet, O. Couture, Z. Lenkei, and M. Tanter, "Transcranial functional ultrasound imaging of the brain using microbubble-enhanced ultrasensitive doppler," *NeuroImage*, vol. 124, no. Pt A, pp. 752–761, 2015.
- [4] K. B. Hansen, C. A. Villagmez-Hoyos, J. C. Brasen, K. Diamantis, V. Sboros, C. M. Srensen, and J. A. Jensen, "Robust microbubble tracking for super resolution imaging in ultrasound," in *Proc. IEEE Ultrason. Symp.*, Sept 2016, pp. 1–4.
- [5] K. Christensen-Jeffries, S. Harput, J. Brown, P. N. T. Wells, P. Aljabar, C. Dunsby, M. X. Tang, and R. J. Eckersley, "Microbubble axial localization errors in ultrasound super-resolution imaging," *IEEE Trans. Ultrason., Ferroelectr., Freq. Control*, vol. 64, no. 11, pp. 1644–1654, Nov. 2017.
- [6] P. Song, A. Manduca, J. D. Trzasko, R. E. Daigle, and S. Chen, "On the effects of spatial sampling quantization in super-resolution ultrasound microvessel imaging," *IEEE Trans. Ultrason., Ferroelectr., Freq. Control*, pp. 1–1, 2018.
- [7] K. Diamantis, A. Greenaway, T. Anderson, J. A. Jensen, and V. Sboros, "Experimental performance assessment of the sub-band minimum variance beamformer for ultrasound imaging," *Ultrasonics*, vol. 79, pp. 87–95, 2017.
- [8] K. Diamantis, T. Anderson, M. B. Butler, C. A. Villagmez-Hoyos, J. A. Jensen, and V. Sboros, "Resolving ultrasound contrast microbubbles using minimum variance beamforming," *IEEE Trans. Medical Imaging*, pp. 1–1, 2018.
- [9] K. Diamantis, A. Greenaway, T. Anderson, J. Jensen, P. Dalgarno, and V. Sboros, "Super-resolution axial localization of ultrasound scatter using multi-focal imaging," *IEEE Trans. Biomed. Eng.*, vol. 65, no. 8, pp. 1840–1851, July 2018.
- [10] P. A. Dalgarno, H. I. C. Dalgarno, A. Putoud, R. Lambert, L. Paterson, D. C. Logan, D. P. Towers, R. J. Warbuton, and A. H. Greenaway, "Multiplane imaging and three dimensional nanoscale particle tracking in biological microscopy," *Opt. Expr.*, vol. 18, no. 2, pp. 877–884, 2010.
- [11] H. I. C. Dalgarno, P. A. Dalgarno, A. C. Dada, C. E. Towers, G. J. Gibson, R. M. Parton, I. Davis, R. J. Warburton, and A. H. Greenaway, "Nanometric depth resolution from multi-focal images in microscopy," *J. R. Soc. Interface*, vol. 8, no. 60, pp. 942–951, July 2011.
- [12] K. Diamantis, P. A. Dalgarno, A. H. Greenaway, T. Anderson, J. A. Jensen, and V. Sboros, "High resolution depth-resolved imaging from multi-focal images for medical ultrasound," in *Proc. IEEE Eng. in Med. and Biol. Soc.*, 2015, pp. 7067–7070.
- [13] R. A. Muller and A. Buffington, "Real-time correction of atmospherically degraded telescope images through image sharpening," *J. Opt. Soc. Am.*, vol. 64, no. 9, pp. 1200–1210, Sep. 1974.
- [14] W. Marczak, "Water as a standard in the measurements of speed of sound in liquids," *J. Acoust. Soc. Am.*, vol. 102, no. 5, pp. 2776–2779, 1997.
- [15] J. A. Jensen, H. Holten-Lund, R. T. Nilsson, M. Hansen, U. D. Larsen, R. P. Domsten, B. G. Tomov, M. B. Stuart, S. I. Nikolov, M. J. Pihl, Y. Du, J. H. Rasmussen, and M. F. Rasmussen, "SARUS: A synthetic aperture real-time ultrasound system," *IEEE Trans. Ultrason., Ferroelectr., Freq. Control*, vol. 60, no. 9, pp. 1838–1852, 2013.
- [16] J. M. Hansen, M. C. Hemmsen, and J. A. Jensen, "An object-oriented multi-threaded software beam formation toolbox," in *Proc. SPIE Med. Imag.*, vol. 79680Y, Mar. 2011. [Online]. Available: 10.1117/12.878178.